POLITECNICO MILANO 1863

SCUOLA DI INGEGNERIA INDUSTRIALE E DELL'INFORMAZIONE

EXECUTIVE SUMMARY OF THE THESIS

Advanced Methods for Multi-Encounter Conjunction Assessment

LAUREA MAGISTRALE IN SPACE ENGINEERING - INGEGNERIA SPAZIALE

Author: Alejandro Álvarez Salazar

Advisor: Prof. Pierluigi Di Lizia

Co-advisor: Dr. Diego Escobar Antón, Diego Aranda Pradana, Jorge Rubio Antón

Academic year: 2025-26

---

1. Introduction

As the number of objects in Low Earth Orbit (LEO) continues to grow, collision avoidance has become a frequent and complex operational challenge. The increasing density of space debris and active constellations frequently results in multi-encounter scenarios, where a single operational satellite faces multiple potential collisions within a short prediction horizon [1]. Traditionally, Space Surveillance and Tracking (SST) operations process these conjunctions as isolated events. However, mitigating risks individually without considering the global context may lead to operational inefficiencies and excessive propellant consumption [2]. Therefore, a transition from single-event assessment to global risk estimation is required to support operational safety and optimize collision avoidance manoeuvres.

1.1. State of the Art

The assessment of orbital safety is based on the detection and evaluation of physical conjunctions. A conjunction is defined as the event where the relative distance between two space objects reaches a global minimum, known as the Time of Closest Approach (TCA) [3]. At this exact instant, assuming rectilinear relative motion, the relative position vector is strictly orthogonal to the relative velocity vector.

Because the state vectors of the objects are subject to uncertainties, the exact miss distance cannot be determined. Instead, the operational risk is quantified probabilistically. The standard approach, formulated by Akella and Alfriend [3], projects the three-dimensional Gaussian uncertainties of both objects onto the conjunction plane (the B-plane), which is perpendicular to the relative velocity. The Probability of Collision (P_c) is then evaluated by integrating the resulting 2D probability density function over the combined Hard-Body Radius (R) of the objects. The probability is computed as:

$$P_c = \frac{1}{2\pi\sqrt{|P_\perp|}} \iint \exp\left(-\frac{1}{2}\mathbf{\Delta}^\mathsf{T} P_\perp^{-1}\mathbf{\Delta}\right) d\mathbf{x} \quad (1)$$

where $\mathbf{x} = [\xi, \eta]^\mathsf{T}$ is the projected relative position, $\mathbf{\Delta} = \mathbf{x} - \mathbf{x}_0$ is the deviation from the nominal miss distance $\mathbf{x}_0$, $P_\perp$ is the projected relative covariance matrix, and $D = \{(\mathbf{x}) : \|\mathbf{x}\| \leq R\}$ This analytical method is computationally efficient and is widely used in modern SST operations. However, this metric is designed to evaluate individual events in isolation. When dealing with multi-event scenarios, standard operational frameworks need to combine these individual P_c values into a unified metric of total risk. To

manage the unknown statistical correlation between consecutive encounters, the assessment is bounded by the Fréchet-Hoeffding inequalities [4].
The theoretical lower bound assumes maximum overlap between events (i.e., total positive correlation), while the upper bound assumes the events are mutually exclusive, leading to a simple summation approximation [5]. These limits strictly bound the Total Probability of Collision (TPoC) for N events:

$$\max_{i=1}^{N}\{P(A_i)\} \leq P \leq \min\left(1, \sum_{i=1}^{N} P(A_i)\right) \tag{2}$$

Because current analytical tools primarily provide individual probabilities ($P(A_i)$), an alternative operational approach estimates the total risk by assuming complete statistical independence between the events, calculating the product of survival probabilities:

$$TPoC \approx 1 - \prod_{i=1}^{N}(1 - P(A_i)) \tag{3}$$

However, both the summation bound and the independence assumption may introduce inaccuracies in operations. Statistical dependence between encounters is generated by two primary mechanisms. First, the initial state uncertainty of the common satellite propagates coherently across all successive events, physically linking the position errors. Second, uncertainties in the dynamic propagation models, particularly atmospheric drag, act as a common process noise that simultaneously affects the trajectories of all involved objects over the analysis window [6, 7].
These shared sources of error invalidate the independence hypothesis [8]. Consequently, to prevent both the overestimation of risk and the execution of unnecessary collision avoidance manoeuvres, it is necessary to develop advanced analytical frameworks that compute the exact joint collision probability by directly modelling the present correlations.

1.2. Problem Statement

This thesis focuses on the accurate quantification of the total collision risk in correlated multi-encounter scenarios. For the sake of simplicity, the problem is restricted to sequences of two events, A_1 and A_2, occurring in a short period of time within LEO. The total risk is defined as the probability of the union of these events, which is expanded using the inclusion-exclusion principle [9]:

$$P(A_1 \cup A_2) = P(A_1) + P(A_2) - P(A_1 \cap A_2) \tag{4}$$

While individual probabilities $P(A_1)$ and $P(A_2)$ are computed using standard analytical methods, the main challenge is the determination of the joint probability $P(A_1 \cap A_2)$. To account for the physical correlation, a global state vector $\mathbf{x}$ is constructed by concatenating the relative position vectors of both encounters. If $\mathbf{r}_p(t_i)$ represents the position of the primary satellite and $\mathbf{r}_{s_i}(t_i)$ represents the position of the i-th secondary object at epoch t_i, the global state vector is defined as:

$$\mathbf{x} = \begin{bmatrix} \boldsymbol{\rho}_1 \\ \boldsymbol{\rho}_2 \end{bmatrix} = \begin{bmatrix} \mathbf{r}_{s_1}(t_1) - \mathbf{r}_p(t_1) \\ \mathbf{r}_{s_2}(t_2) - \mathbf{r}_p(t_2) \end{bmatrix} \tag{5}$$

The associated global covariance matrix explicitly models the cross-correlation generated by the common states and the shared atmospheric drag uncertainties:

$$\boldsymbol{\Sigma} = \begin{bmatrix} \boldsymbol{\Sigma}_{11} & \boldsymbol{\Sigma}_{12} \\ \boldsymbol{\Sigma}_{21} & \boldsymbol{\Sigma}_{22} \end{bmatrix} \tag{6}$$

The joint probability is thus obtained by integrating the multivariate joint probability density function over the respective collision domains ($\mathcal{D}_1$ and $\mathcal{D}_2$):

$$P(A_1 \cap A_2) = \int_{\mathcal{D}_1} \int_{\mathcal{D}_2} \mathcal{N}(\mathbf{x}; \boldsymbol{\mu}, \boldsymbol{\Sigma})\, d\mathbf{x} \tag{7}$$

By evaluating scenarios involving distinct secondaries, repeated encounters, and environmental perturbations, the overestimation or underestimation of the collision risk introduced by traditional operational assumptions is mathematically evaluated.

2. Methodology

To accurately compute the total collision risk in multi-encounter scenarios, a progressive analytical framework is proposed. Before studying the full three-dimensional orbital mechanics, a simplified two-dimensional formulation—referred to as the "Toy Problem"—has been developed. This preliminary step isolates the fundamental sources of statistical correlation, verifying that the presence common uncertainties force the joint probability to deviate from the simple product of independent marginals. Building upon these statistical principles, the framework is generalized to address 3D orbital dynamics.

2.1. Two-Dimensional Toy Problem

The baseline 2D scenario consists of a primary vehicle moving along a longitudinal axis, encountering two secondary objects (pedestrians $i \in \{1, 2\}$) crossing its path at different epochs (t_1 and t_2). The relative lateral distance at the crossing time is defined as $z_i \equiv x_{p,i}(t_i) - x_v(t_i)$. A collision event ($A_i$) is triggered when this distance falls below a Hard-Body threshold (W), such that $A_i = \{|z_i| < W\}$.

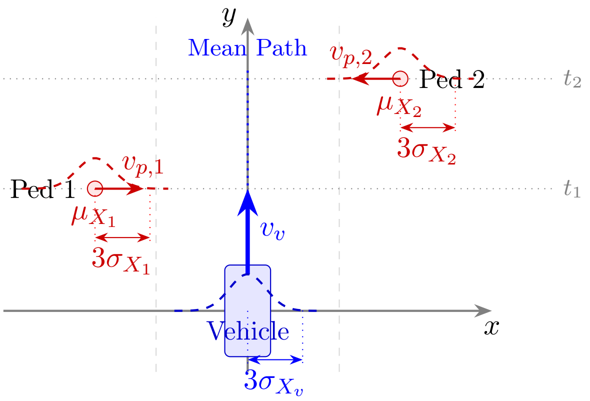

Figure 1: "Toy Problem" configuration.

By progressively introducing uncertainty sources, the mathematical behaviour of the joint probability has been evaluated as:

$$P(A_1 \cap A_2) = \iint_{\mathcal{D}} f(z_1, z_2)\, dz_1\, dz_2 \qquad (8)$$

where the integration domain $\mathcal{D}$ is defined by the lateral limits of both collisions:

$$\mathcal{D} = \{(z_1, z_2) : |z_1| < W,\ |z_2| < W\} \qquad (9)$$

2.1.1 Cases of Study

The analytical resolution demonstrated that if all initial positions are strictly independent and the vehicle is deterministic, the covariance between events is zero ($\text{Cov}(Z_1, Z_2) = 0$), allowing the joint probability integral to factorize into independent components ($P(A_1 \cap A_2) = P(A_1)P(A_2)$). However, realistic shared uncertainties generate the following specific correlation structures:

Common Primary Uncertainty. Introducing initial positional uncertainty to the vehicle ($X_v \sim \mathcal{N}(\mu_{X_v}, \sigma^2_{X_v})$) statistically couples the relative distances Z_1 and Z_2. The covariance evaluates strictly to the primary's variance:

$$\text{Cov}(Z_1, Z_2) = \sigma^2_{X_v} \qquad (10)$$

Because $\rho \neq 0$, the joint probability integral cannot be evaluated as a simple product. Instead, it must be solved using a conditional probability factorization ($f_{Z_1,Z_2} = f_{Z_1} f_{Z_2|Z_1}$). This transforms the calculation into a nested integral, where the mean and variance of the second event are updated based on the first (z_1). This mathematical decoupling establishes the approach for the 3D orbital case, where the primary's state error will link the consecutive conjunctions.

Repeated Secondary Encounters. When the primary intersects the identical secondary object (X_p) twice, the shared pedestrian uncertainty further increases the cross-covariance:

$$\text{Cov}(Z_1, Z_2) = \sigma^2_{X_v} + \sigma^2_{X_p} \qquad (11)$$

In this limit situation , the correlation coefficient approaches unity ($\rho \to 1$). Consequently, the conditional variance collapses towards zero, and the conditional PDF approximates a Dirac delta function. The 2D joint integral simplifies into a single 1D integration over the marginal distribution of the first event, as the second collision becomes a deterministic geometric condition.

Environmental Disturbances. A common external perturbation, modelled as a "wind" field $W \sim \mathcal{N}(0, \sigma^2_W)$, was introduced, affecting objects based on kinematic sensitivity coefficients (k_i). This shared dynamic noise creates an additional covariance term:

$$\text{Cov}(Z_1, Z_2) = \sigma^2_{X_v} + k_1 k_2 \sigma^2_W \qquad (12)$$

Even if the initial states of all objects are perfectly independent, this external force couples the events. The integration requires the full bivariate normal formulation, and the conditional probability factorization, where the correlation strength is strictly modulated by how sensitive each object is to the wind (k_1, k_2). In LEO scenarios, this effect represents the physical analogue of atmospheric density errors, which add a targeted bias to the global covariance matrix.

These findings suggest that the joint probability must be evaluated using conditional probability frameworks. Consequently, the 3D methodology requires a global covariance matrix capable of capturing state propagations and environmental sensitivities across multiple epochs.
The advanced analytical resolution developed for the 3D orbital space is structured into a mathematical pipeline: the formulation of the high-dimensional joint integral, the geometric reduction of the problem space using B-plane projections, the statistical decoupling of the integration domain through the Schur complement, and finally, the construction of the global covariance matrix.

2.2. Full Joint Probability Integral

The two-dimensional "Toy Problem" established that the joint probability of two correlated collision events (A_1 and A_2) is obtained by integrating the bivariate normal Probability Density Function (PDF) over the respective lateral collision domains [10].
Extrapolating this logic directly to 3D orbital mechanics, the relative position between the primary and the k-th secondary object at the Time of Closest Approach (t_k) becomes a 3D random vector: $\mathbf{z}_k = \mathbf{r}_{s_k}(t_k) - \mathbf{r}_p(t_k)$. Consequently, the joint probability $P(A_1 \cap A_2)$ requires a 6D integration of the multivariate normal distribution over the two spatial collision volumes defined by the respective Hard-Body Radii (R_1 and R_2):

$$P(A_1 \cap A_2) = \iiiint \iint_{\mathcal{D}} f(\mathbf{z})\, d\mathbf{z}_1 d\mathbf{z}_2 \quad (13)$$

where $\mathcal{D} = \{(\mathbf{z}_1, \mathbf{z}_2) \mid \|\mathbf{z}_1\| < R_1, \|\mathbf{z}_2\| < R_2\}$ and $f(\mathbf{z})$ is governed by the 6×6 global covariance matrix $\mathbf{\Sigma}_Z$ capturing the physical correlation between the two epochs:

$$\mathbf{\Sigma}_Z = \begin{bmatrix} \mathbf{\Sigma}_{Z_1} & \mathbf{\Sigma}_{Z_{1,2}} \\ \mathbf{\Sigma}_{Z_{2,1}} & \mathbf{\Sigma}_{Z_2} \end{bmatrix} \quad (14)$$

2.3. Dimensionality Reduction

Solving a 6D integral numerically is computationally demanding for routine operations. To improve efficiency, the classical Akella-Alfriend dimensionality reduction is extended to the double-conjunction scenario. This method leverages the assumption that relative motion is rectilinear and velocities remain constant during the brief duration of each individual encounter.

For each encounter i, an orthogonal conjunction frame is defined. The $\boldsymbol{\eta}_i$ axis is aligned with the relative velocity $\boldsymbol{\nu}(t_i)$, while the orthonormal basis $\{\boldsymbol{\xi}_i, \boldsymbol{\zeta}_i\}$ defines the B-plane (the plane orthogonal to the relative velocity). The transformation matrix $\mathbf{C}_i$ maps vectors from the inertial frame to this conjunction frame:

$$\mathbf{C}_i = \begin{bmatrix} \boldsymbol{\eta}_i^\top \\ \boldsymbol{\xi}_i^\top \\ \boldsymbol{\zeta}_i^\top \end{bmatrix} \quad (15)$$

A projection matrix $\mathbf{T}^*$ is then applied to extract only the components within the B-plane, removing the component along the relative velocity. To apply this to the joint 6D problem, a combined transformation matrix $\mathbf{T}$ is defined to simultaneously rotate and project the relative position vectors and the global covariance matrix onto their respective B-planes:

$$\mathbf{T} = \begin{bmatrix} \mathbf{T}^*\mathbf{C}_1 & \mathbf{0} \\ \mathbf{0} & \mathbf{T}^*\mathbf{C}_2 \end{bmatrix} \quad (16)$$

This operation effectively reduces the 3D collision volumes into 2D circular cross-sections, transforming the full spatial covariance into a 4×4 projected matrix without losing probability information:

$$\mathbf{\Sigma}_Z^* = \mathbf{T}\mathbf{\Sigma}_Z\mathbf{T}^\top = \begin{bmatrix} \mathbf{\Sigma}_{Z_1}^* & \mathbf{\Sigma}_{Z_{1,2}}^* \\ \mathbf{\Sigma}_{Z_{1,2}}^{*\top} & \mathbf{\Sigma}_{Z_2}^* \end{bmatrix} \quad (17)$$

where the superscript $*$ denotes variables projected onto the 2D conjunction planes. This reduces the mathematical problem to a 4D integral.

2.4. Statistical Decoupling

While the problem is successfully reduced to 4D, the integration over the two disjoint circular collision domains remains statistically coupled by the off-diagonal correlation block $\mathbf{\Sigma}_{Z_{1,2}}^*$. To decouple the integral physically and mathematically, the Schur complement factorization is applied to the projected covariance matrix [11].
This theorem allows the 4D Joint PDF to be factorized into a marginal PDF for the first event ($f_{Z_1}^*$) and a conditional PDF for the second event ($f_{Z_2|Z_1}^*$). The conditional covariance of the second encounter, known as the Schur complement, is given by:

$$\mathbf{\Sigma}_{Z_2|Z_1}^* = \mathbf{\Sigma}_{Z_2}^* - \mathbf{\Sigma}_{Z_{21}}^* \mathbf{\Sigma}_{Z_1}^{*-1} \mathbf{\Sigma}_{Z_{12}}^* \quad (18)$$

Furthermore, the expected location of the second event is dynamically shifted as a linear function of the position of the first encounter ($\mathbf{z}_1^*$):

$$\boldsymbol{\mu}^*_{Z_2|Z_1} = \boldsymbol{\mu}^*_{Z_2} + \boldsymbol{\Sigma}^*_{Z_{21}}\boldsymbol{\Sigma}^{*-1}_{Z_1}(\mathbf{z}_1^* - \boldsymbol{\mu}^*_{Z_1}) \tag{19}$$

Through the Schur factorization, the coupled 4D integral is efficiently transformed into two nested 2D integrals:

$$P(A_1 \cap A_2) = \iint_{D_1} f^*_{Z_1}(\mathbf{z}_1^*) \iint_{D_2} f^*_{Z_2|Z_1}\, d\mathbf{z}_2^* d\mathbf{z}_1^* \tag{20}$$

Where $D_i = (\mathbf{z}_i^*) : \|\mathbf{z}_i^*\| < R_i$ for $i \in \{1, 2\}$. Here, the outer integral evaluates the marginal probability of the first conjunction over its B-plane, while the inner integral computes the conditional probability of the second conjunction given a particular geometric realization of $\mathbf{z}_1^*$. To resolve this expression, a dynamic numerical meshing strategy is implemented. The continuous integration domains are discretized into finite summations, with the grid resolution adapting dynamically based on the Hard-Body Radius and the magnitude of the covariance matrices.

2.5. Construction of the Global Covariance Matrix

The utility of the entire integration and decoupling process relies on the characterization of the 6×6 unprojected global covariance matrix $\boldsymbol{\Sigma}_Z$.

2.5.1 Diagonal Blocks

The diagonal blocks represent the total covariance of the relative position vector at each encounter evaluated independently. This matrix combines the propagated state covariances of the primary ($\boldsymbol{\Sigma}_{r_p}$) and the specific secondary object ($\boldsymbol{\Sigma}_{r_s}$), augmented by the correlated environmental uncertainty. Using the relative sensitivity vector $\mathbf{S}_{rel,k}$, which quantifies the displacement caused by atmospheric density errors (σ_ρ^2), the diagonal covariance is given by:

$$\boldsymbol{\Sigma}_{Z_k} = \boldsymbol{\Sigma}_{r_{sk}}(t_k) + \boldsymbol{\Sigma}_{r_p}(t_k) + \mathbf{S}_{rel,k}\mathbf{S}^\top_{rel,k}\sigma_\rho^2 \tag{21}$$

2.5.2 Off-Diagonal Block

The off-diagonal cross-correlation block ($\boldsymbol{\Sigma}_{Z_{1,2}}$) represents the physical coupling between t_1 and t_2. To map the uncertainty from the first encounter to the second, the orbital dynamics are linearized using the State Transition Matrix (STM), denoted as $\boldsymbol{\Phi}(t_2, t_1)$. Expanding the covariance expectation yields three distinct correlation mechanisms:

1. **Primary State Correlation:** The initial state error of the common primary satellite propagates between t_1 and t_2.
2. **Secondary State Correlation:** If the primary encounters the identical secondary object twice, the secondary's state error also propagates. If $s_1 \neq s_2$, this term vanishes.
3. **Environmental Correlation:** Errors in atmospheric density predictions act as a common bias affecting the trajectories of all involved objects over the analysis interval.

Combining these three effects, the complete analytical expression for the cross-correlation block is defined as:

$$\begin{aligned} \boldsymbol{\Sigma}_{Z_{1,2}} = {} & \underbrace{\left[\boldsymbol{\Sigma}_{r_p}\boldsymbol{\Phi}^\top_{r_p} + \boldsymbol{\Sigma}_{rv_p}\boldsymbol{\Phi}^\top_{rv_p}\right]}_{\text{Primary}} \\ & + \underbrace{\left[\boldsymbol{\Sigma}_{r_s}\boldsymbol{\Phi}^\top_{r_s} + \boldsymbol{\Sigma}_{rv_s}\boldsymbol{\Phi}^\top_{rv_s}\right]}_{\text{Secondary (If repeated)}} \\ & + \underbrace{\mathbf{S}_{rel,1}\mathbf{S}^\top_{rel,2}\sigma_\rho^2}_{\text{Environmental}} \end{aligned} \tag{22}$$

where all covariance matrices $\boldsymbol{\Sigma}$ are evaluated at time t_1, and all state transition matrices $\boldsymbol{\Phi}$ propagate the state from t_1 to t_2.

2.5.3 Theoretical Bounds of the Conditional Covariance

The mathematical variance reduction (Eq. (18)) and the spatial displacement of the conditional mean (Eq. (19)) jointly represent the physical coupling between events. The behaviour of this statistical formulation is governed by the matrix construction defined above:

Case 1: Influence of the Primary Object. When interacting with distinct secondary objects, the variance reduction and mean displacement are determined by the relative magnitudes of the covariances. If the secondary uncertainties dominate ($\mathcal{O}(\boldsymbol{\Sigma}_{r_p}) \ll \mathcal{O}(\boldsymbol{\Sigma}_{r_s})$), the variance reduction and mean shift are minimal, allowing the joint integral to be closely approximated by the product of independent probabilities ($P_1 P_2$). If the covariances are balanced

($\mathcal{O}(\mathbf{\Sigma}_{r_p}) \approx \mathcal{O}(\mathbf{\Sigma}_{r_s})$), a noticeable partial reduction occurs. Finally, if the primary's covariance dominates ($\mathcal{O}(\mathbf{\Sigma}_{r_p}) \gg \mathcal{O}(\mathbf{\Sigma}_{r_s})$), the Schur reduction term scales directly with the primary covariance, and the conditional mean $\boldsymbol{\mu}^*_{Z_2|Z_1}$ shifts significantly. However, the total vanishing of $\mathbf{\Sigma}^*_{Z_2|Z_1}$ is not possible; the independent contribution of the second secondary object establishes a strictly positive lower bound. In this dominant regime, the joint integral diverges notably from the independent assumption, requiring the full nested evaluation.

Case 2: Re-encounter with the Same Secondary. In an ideal, unperturbed Keplerian case where STMs approximate the identity matrix (exactly the same encounter one period later), the cross-terms cancel the diagonal block, reducing the conditional covariance towards the null matrix ($\mathbf{\Sigma}^*_{Z_2|Z_1} \to \mathbf{0}$). In this theoretical limit, the second conditional PDF converges to a Dirac delta function $\delta(\mathbf{z}^*_2 - \boldsymbol{\mu}^*_{Z_2|Z_1})$, where the conditional mean deterministically maps the spatial deviation of the first event to the second. This effect collapses the complex nested integral into a simpler evaluation governed primarily by the first event's marginal distribution. Under realistic conditions, orbital perturbations and STM deviations prevent perfect cancellation, leaving a reduced but strictly positive definite dispersion. This case presents the most extreme results, going from a totally negative correlation between events, leading to a null joint probability (upper Fréchet-Hoeffding bound), to a full positive correlation, obtaining a near-total overlap between the events (lower Fréchet-Hoeffding bound) depending on how the displaced conditional mean aligns with the second collision geometry.

Case 3: Environmental Uncertainty. The atmospheric error covariance matrices are constructed by multiplying a sensitivity column vector by a row vector, producing a matrix with a rank of one. Physically, this means the position uncertainty added by drag only moves along a single line. Consequently, the mathematical subtraction in the Schur complement only operates along that exact direction, leaving orthogonal directions completely unaffected. Similarly, the conditional mean $\boldsymbol{\mu}^*_{Z_2|Z_1}$ is exclusively displaced along this specific aerodynamic axis. Thus, atmospheric correlation alone cannot reduce the conditioned covariance to zero. As a result, the joint probability integral becomes directionally coupled, modifying the final collision risk only if the relative B-plane geometries align with this specific perturbation line.

3. Results

This section presents the numerical validation and analytical results obtained from the models developed in this thesis. The analysis is divided into two main sections: the evaluation of the simplified two-dimensional "Toy Problem" to establish fundamental physical behaviours, and the application of the full three-dimensional orbital model to realistic multi-event scenarios.

3.1. Two-Dimensional Toy Problem Results

The evaluation of the "Toy Problem" yielded valuable insights regarding the physical drivers of statistical correlation. To validate the analytical expressions, Monte Carlo simulations were performed. The required number of samples N was estimated to ensure statistical convergence using the standard formula for confidence intervals [12]:

$$N \geq \frac{Z^2_{1-\alpha/2}(1-P_c)}{\epsilon^2 P_c} \tag{23}$$

For a confidence level of 95% ($Z \approx 1.96$), an expected probability of collision on the order of 10^{-2}, and a relative error of $\epsilon = 1\%$, the necessary sample size was determined to be on the order of 10^7. With this setup, the theoretical limits of the probability of the union Eq. (2) were verified across all experiments.

The analysis encompassed the sequential scenarios introduced in Section 2: independent objects (Case 1), an uncertain primary vehicle inducing coupling (Case 2), a repeated secondary object presenting a correlation limit (Case 3), explicitly correlated secondary objects (Case 4), and a common environmental disturbance (Case 5). A comprehensive numerical overview is presented in Table 1, illustrating how the independent assumption systematically fails as shared uncertainty increases.

Based on these numerical results, the impact of correlation was found to be highly dependent on the relative geometry of the encounters. Figure

Table 1: Summary of the 2D "Toy Problem" results. The analytical TPoC is compared against the simplified independent assumption.
Legend: **a**: Same-Side geometry; **b**: Opposite-Side geometry. Roman numbers (**i-iv**) denote progressive parameter variations: increasing vehicle uncertainty (Cases 2 and 5), and decreasing correlation strength (Case 4).

Case	Conf.	Anal. TPoC [-]	Simp. TPoC [-]	Rel. Err [%]
Case 1	-	0.0342	0.0342	∼0.00
Case 2	a.i	0.0220	0.0220	0.04
	a.ii	0.0904	0.0989	9.42
	a.iii	0.2426	0.3175	30.80
	b.i	0.0221	0.0220	0.03
	b.ii	0.1012	0.0989	2.26
	b.iii	0.3465	0.3175	8.38
Case 3	a	0.0300	0.0435	44.70
	b	0.0169	0.0169	0.39
Case 4	a.i	0.0242	0.0281	16.00
	a.ii	0.0273	0.0281	2.78
	a.iii	0.0283	0.0281	0.65
	a.iv	0.0283	0.0281	0.70
	b.i	0.0283	0.0281	0.70
	b.ii	0.0283	0.0281	0.65
	b.iii	0.0273	0.0281	2.78
	b.iv	0.0242	0.0281	16.00
Case 5	a.i	0.0565	0.0558	1.24
	a.ii	0.1295	0.1337	3.26
	a.iii	0.2696	0.3279	21.60
	b.i	0.0537	0.0558	3.85
	b.ii	0.1364	0.1337	1.98
	b.iii	0.3584	0.3279	8.51

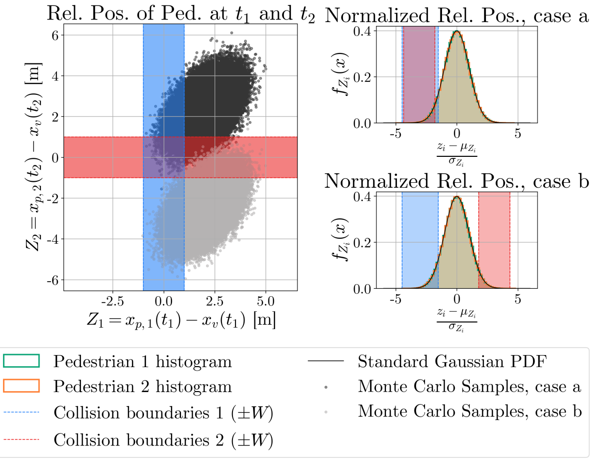

Figure 2: The two fundamental geometric configurations evaluated: Same-Side (case a) where both events occur on the same lateral side of the primary's path, and Opposite-Side (case b) where they occur on alternating sides. This difference produces a shift of the relative positions results obtained from the Monte Carlo method, varying the number of samples that enters into the double collision area

2 visually represents a generic result from Case 2 (Conf. ii), where the geometrical influence is clearly shown.
The relationship between geometry, uncertainty scaling, and the resulting total risk can be summarized in the following patterns:

The Geometry Effect: Same-Side vs. Opposite-Side. The relative error of the independent assumption (P_1P_2) fluctuates drastically depending on whether the events share the same side. When the secondary objects are positioned on the same side of the primary's path (Configuration a), a positive correlation ($\rho > 0$) implies that a deviation leading to a collision in the first event likely triggers a collision in the second. As observed in Table 1, this alignment drives the actual joint probability higher than the independent product. As a result, the independent formula severely overestimates the TPoC. Figure 3 demonstrates how, as the primary's uncertainty (σ_{X_v}) increases in Case 2, the actual risk approaches the theoretical lower bound, drifting away from the summation formula. Figure 4 corroborates this by showing that directly increasing positive correlation (Case 4) steadily reduces the accumulated risk.

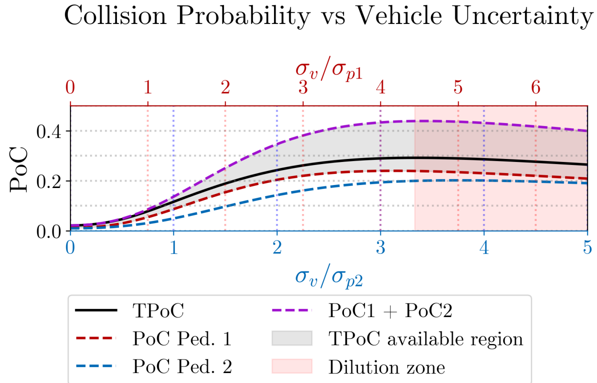

Figure 3: Case 2 (Same-Side): TPoC evolution. The actual risk shifts towards the lower limit as primary uncertainty grows.

Conversely, if the secondary objects are located on opposite sides of the primary's nominal path (Configuration b), a positive correlation implies

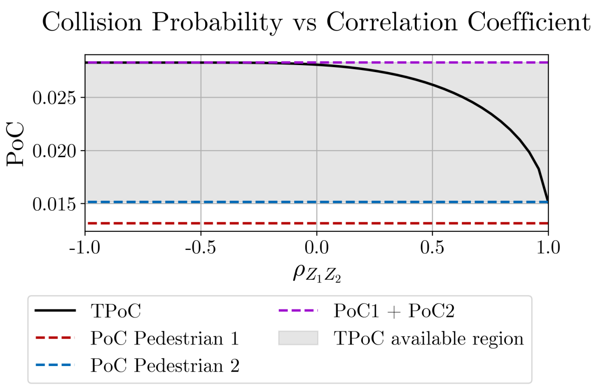

Figure 4: Case 4 (Same-Side): TPoC as a function of the imposed correlation (ρ). Positive correlations group the events, reducing risk.

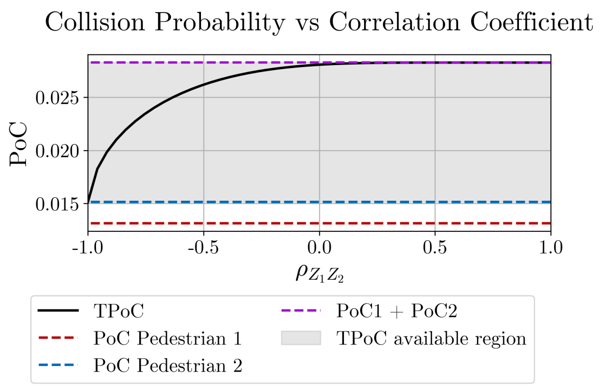

Figure 6: Case 4 (Opposite-Side): The correlation trend is inverted; negative ρ reduces total risk.

that a deviation towards the first object moves the primary away from the second. The events tend to become mutually exclusive ($P_{1\cap 2} \to 0$). In this specific geometry, the simple summation formula ($P_1 + P_2$) provides an accurate estimate of the TPoC. Figure 5 demonstrates how the TPoC remains aligned with the upper bound regardless of the primary's uncertainty. Figure 6 shows an inverted trend for Case 4: negative correlations group the events and lower the total risk.

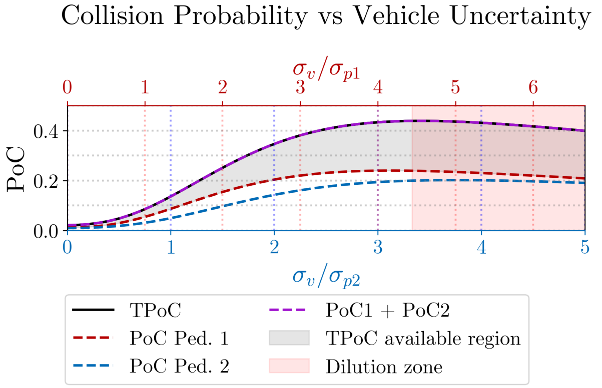

Figure 5: Case 2 (Opposite-Side): TPoC remains aligned with the simple summation upper bound as events become mutually exclusive.

The Correlation Limit ($\rho \to 1$). Case 3 explored the extreme scenario of the primary intersecting the exact same secondary object twice. This physical condition forces the correlation coefficient to approach unity. In this limit, the conditional probability density approximates a deterministic line, indicating that the second event's occurrence is strictly dictated by the spatial outcome of the first. In the Same-Side configuration, this nested geometry forces the joint probability to equate the minimum of the individual probabilities ($P_{1\cap 2} \approx P_1$), as depicted by the collapsed variance in Figure 7. Here, the independent approximation fails drastically, yielding a relative error of 44.7%.

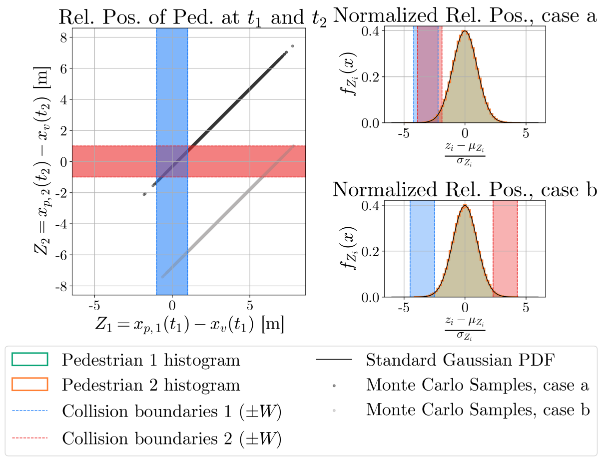

Figure 7: Monte Carlo validation for Case 3 (Repeated Secondary). The samples align along a deterministic path, visually demonstrating the collapse of the conditional variance.

Environmental Perturbations and Coupled Errors. Case 5 introduces a common wind disturbance (W). The results highlighted the shifting nature of correlation. When the wind variance dominates (Configuration i), the correlation is modulated strictly by the relative aerodynamic sensitivities (k_i) of the objects, but

the error achieved is lower than the obtained when the vehicle's uncertainty dominates. However, as the vehicle's position uncertainty increases (Configuration *iii*), the common position error begins to dominate the covariance matrix, and the scenario reverts to the highly correlated behaviour observed in Case 2. In this vehicle-dominated regime, the independent approximation error scales up significantly, reaching 21.6% in the Same-Side geometry (Table 1).
These 2D results confirm that the independent approximation fails systematically depending on the geometric configuration and the origin of the correlation. These observations establish the physical baseline for the complete 3D orbital analysis.

3.2. Three-Dimensional Problem Results

This section numerically validates the extensive theoretical results derived from the previous analytical framework. But before the parametric analysis, the methodology has been validated against a Monte Carlo (MC) simulation over a selected multi-event scenario. To ensure statistical convergence, the required number of samples was estimated using the Dagum bound formulation (Eq. (23)) [12]. Considering an expected collision probability on the order of 10^{-2}, a target relative error of 10%, and a 95% confidence interval, the necessary sample size was determined to be 10^5. The comparison between the empirical results and the analytical integration yielded a relative error for the Total Probability of Collision (TPoC) of 1.33%. As this deviation remains well within the defined statistical margins, the validity of the B-plane projection and the Schur complement decoupling methods is confirmed for the operational 3D environment.
To evaluate the operational impact of neglecting inter-event correlations, the model was applied to two main scenarios: the influence of a common primary object (Case 1) across different uncertainty regimes, and the effect of encountering a repeated secondary object (Case 2) under ideal and perturbed conditions. A comprehensive overview of the analytical results and the relative errors introduced by the standard operational approximation is presented in Table 2.
The numerical results outlined in Table 2 provide a clear indication of how orbital geometry and uncertainty scaling influence the final risk metrics. These behaviours can be analysed sequentially:

Table 2: Summary of the 3D orbital multi-encounter results focusing on the Total Probability of Collision (TPoC). The analytical TPoC is compared against the simplified independent assumption ($P_1 + P_2 - P_1 P_2$).

Case	Configuration	Anal. TPoC [-]	Simp. TPoC [-]	Rel. Err [%]
Case 1: Common Primary	A (Dominant Sec.)	0.536	0.540	0.63
	B (Balanced)	0.508	0.522	2.71
	C (Dominant Pri.)	0.442	0.471	6.53
Case 2: Repeated Sec.	Ideal Unperturbed	0.067	0.127	89.56
	Realistic Perturbed	0.138	0.137	1.23

Analysis of the Common Primary Object (Case 1). This scenario evaluates a single primary satellite encountering two distinct secondary objects, where the statistical coupling is driven by the primary object's initial state uncertainty. The data suggests that the validity of standard operational metrics is highly dependent on the relative covariance regimes.
In Configuration A ($\|\boldsymbol{\Sigma}_p\| \ll \|\boldsymbol{\Sigma}_s\|$), the small primary covariance introduces limited cross-coupling. As observed in Figure 8, the Schur complement reduction on the second B-plane is minimal, and the assumption of statistical independence yields a relatively low TPoC error (0.63%).

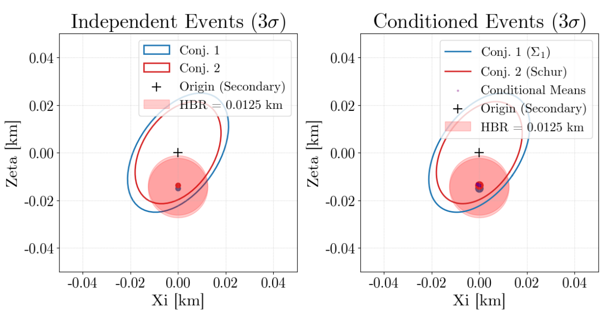

Figure 8: Projection of covariance ellipses onto the B-plane for Configuration A. Given the dominant secondary covariance, the variance reduction and spatial displacement of the conditioned mean are minimal.

However, as the primary covariance grows relative to the secondaries (Configurations B and C, illustrated in Figures 9 and 10), the statistical correlation links the spatial geometries of both events more rigidly.

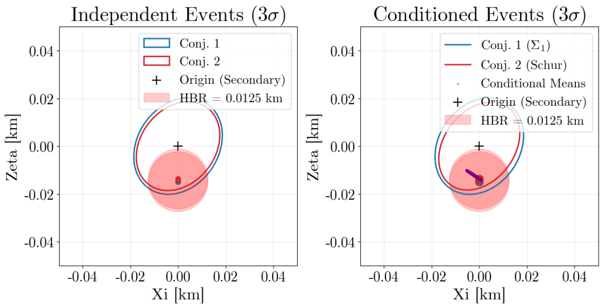

Figure 9: B-plane projection for Configuration B. With balanced covariances, a more noticeable variance reduction and a slight displacement of the conditioned mean begin to appear.

In the primary-dominant regime (Configuration C, Figure 10), treating these events as isolated occurrences leads to an estimation error of 6.53% in the accumulated risk. While this specific TPoC deviation might seem moderate, it stems from a significant underestimation of the joint intersection, indicating that neglecting correlation mathematically forces an overestimation of the total risk. Furthermore, relying on the simple summation bound ($P_1 + P_2$) overestimates the actual risk by more than 20% across all configurations. It should be noted that this substantial deviation arises not only from neglecting the statistical correlation but also from the academic design of the test cases. To ensure numerical precision and clearly observe the coupling effects, the conjunctions designed have been determined to obtain a considerably higher PoC than those typically encountered in routine operations. Consequently, the standard assumption that individual probabilities are sufficiently small to safely neglect their intersection becomes invalid in this context.

Analysis of a Common Secondary Object (Case 2). Case 2 evaluates the correlation generated when the primary satellite encounters the identical secondary object at two successive epochs. Because both objects propagate their initial errors simultaneously, the cross-covariance terms approach the magnitude of the main diagonal blocks, leading to more pronounced statistical dependencies.

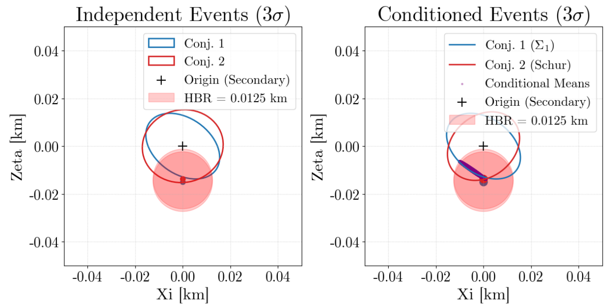

Figure 10: B-plane projection for Configuration C. The dominant primary covariance produces a substantial variance reduction and a highly pronounced spatial displacement of the conditioned mean.

The results illustrate the complex nature of repeated encounters. In the Ideal Unperturbed scenario (Figure 11), the dynamics emulate the correlation limits observed in the 2D "Toy Problem"; the correlation coefficient approaches unity. The conditional covariance practically vanishes, driving the joint probability to roughly equate the minimum of the individual probabilities ($P_{1\cap 2} \approx P_1$). Using the assumption of independence in this theoretical state presents a substantial deviation, heavily overestimating the TPoC with a relative error reaching 89.56%.

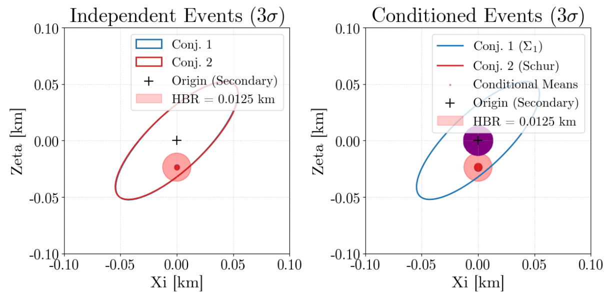

Figure 11: B-plane projection for the Ideal Unperturbed scenario (Case 2, Config A). The conditioned covariance approaches a null matrix, and the conditioned mean dictates the deterministic location of the second encounter.

When realistic orbital perturbations are introduced (Figure 12), the mathematical cancellation of the Schur complement is disrupted. The conditional covariance retains a positive dispersion. More importantly, differential perturbations displace the conditional mean away from the origin in the second B-plane. Depending on the relative trajectory geometry, this spatial displacement can shift the expected location of the second encounter outside the collision volume, driving the joint probability effectively to zero and suggesting the events become mutually exclusive. These dynamics indicate that analytical modelling via Schur decomposition provides a more descriptive framework to estimate the true spatial location and accumulated risk of subsequent encounters in perturbed environments.

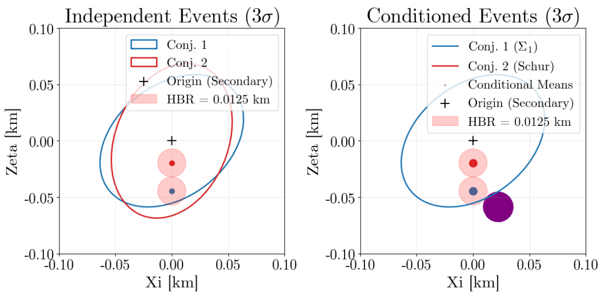

Figure 12: B-plane projection for the Realistic Perturbed scenario (Case 2, Config B). Perturbations and STM deviations prevent perfect cancellation, leaving a strictly positive definite dispersion and displacing the conditional mean.

4. Conclusions

This thesis has presented an analytical approach to evaluate the Total Probability of Collision in scenarios involving multiple orbital encounters. By exploring the physical reasons why uncertainties are shared between events, the proposed mathematical framework offers a more realistic perspective on accumulated risk compared to the traditional assumption of statistical independence. This work aims to provide a solid academic foundation that could eventually support the planning of safer and more efficient collision avoidance manoeuvres.

A significant step in this research was the transition from a simplified two-dimensional model to a complete three-dimensional orbital environment. The initial 2D "Toy Problem" was essential to build intuition, isolate the fundamental causes of statistical correlation, and confirm the basic mathematical behaviours. However, moving to the 3D space revealed a much wider and more complex variety of geometric configurations. In a realistic setting, the way uncertainties evolve over time and how different orbital planes intersect create overlapping risks that cannot be fully captured by simple rules.

Through this analytical lens, a few key behaviours were observed. First, when a primary satellite faces multiple distinct objects, the relationship between the events is heavily influenced by which object carries the most uncertainty. If the primary vehicle's uncertainty is the largest, the encounters tend to become correlated. In such situations, treating them as completely separate events may lead to a noticeable overestimation of the total risk. Second, when a satellite encounters the exact same object more than once, the correlation is inherently strong. However, this connection is highly sensitive to the small variations caused by natural orbital perturbations. These subtle dynamic changes dictate how the geometries align in subsequent encounters, which can drastically alter the final joint probability, making the events either highly nested or mutually exclusive.

Overall, this research has addressed the multi-encounter problem from an operational point of view. But the priority has been to ensure mathematical consistency and a clear understanding of the physical relationships, developing the theoretical groundwork and using academic examples to prove the validity of the method.

4.1. Future Lines of Work

To build upon the theoretical progress achieved in this thesis, two main areas for future research are suggested:

- **Numerical Validation of Environmental Effects:** The analytical ideas developed regarding shared environmental noise, particularly atmospheric drag, would benefit from thorough numerical testing in realistic Low Earth Orbit simulations. The theoretical model suggests that atmospheric density errors create a very specific, single-direction correlation [13] that depends on how similarly the objects react to drag. Interestingly, if the objects share the same physical and aerodynamic properties, this specific relative correlation might even cancel out. Verifying these subtle directional effects through extensive numerical methods is a natural continuation of this study.
- **Extension to Multiple Encounters:** A logical next step is to expand the current

methodology, which focuses on pairs of conjunctions, to sequences involving any number of events. The basic mathematical theory applied here can be generalized to find the triple, quadruple, or higher-order joint probabilities by adding more nested integrals to the formulation. However, it is important to be cautious regarding the computational cost. Calculating these multidimensional integrals demands a significant computational effort. Future work would need to explore advanced numerical integration techniques to manage this processing time while keeping the analytical precision intact.

References

[1] Romain Garmier and Jan Siminski. Collision risk assessment for multiple encounters. *Proceedings of the 8th European Conference on Space Debris*, 2021.

[2] Zeno Pavanello, Laura Pirovano, Roberto Armellin, Andrea De Vittori, and Pierluigi Di Lizia. A convex optimization method for multiple encounters collision avoidance maneuvers. In *AIAA SCITECH 2024 Forum*, Orlando, FL, 2024.

[3] Maruthi R. Akella and Kyle T. Alfriend. The probability of collision between space objects. *Journal of Guidance, Control, and Dynamics*, 23(5):769–772, 2000.

[4] Maurice Fréchet. Généralisation du théorème des probabilités totales. *Fundamenta Mathematicae*, 25(1):379–387, 1935.

[5] Ryan C Frigm, Matthew D Hejduk, Lauren C Johnson, and Dragan Plakalovic. Total probability of collision as a metric for finite conjunction assessment and collision risk management. In *Advanced Maui Optical and Space Surveillance Technologies (AMOS) Conference*, Maui, HI, 2014.

[6] Stephen J Casali, Doyle T Hall, Daniel E Snow, Matthew D Hejduk, Lauren C Johnson, Bruce B Skrehart, and Luis G Baars. Effect of cross-correlation of orbital error on probability of collision determination. In *AAS/AIAA Astrodynamics Specialist Conference*, number AAS 18-272, Snowbird, UT, 2018.

[7] NASA. Nasa conjunction assessment handbook, appendix n: Pc calculation approaches. NASA CARA Program, 2024. Update 3/20/24.

[8] Doyle T Hall, Luis G Baars, and Stephen J Casali. A multistep probability of collision computational algorithm. In *AAS/AIAA Astrodynamics Specialist Conference*, AAS 23-398, Big Sky, MT, 2023.

[9] George Boole. *An Investigation of the Laws of Thought on Which are Founded the Mathematical Theories of Logic and Probabilities*. Walton and Maberly, London, 1854.

[10] Arak M. Mathai and Hans J. Haubold. *Probability and Statistics: A Course for Physicists and Engineers*. Walter de Gruyter / De Gruyter Open, 2018. Open access edition; freely available PDF via De Gruyter Open / OER portals.

[11] Fuzhen Zhang, editor. *The Schur Complement and Its Applications*, volume 4 of *Numerical Methods and Algorithms*. Springer, 2005.

[12] Salvatore Alfano. Satellite conjunction monte carlo analysis. In *AAS/AIAA Astrodynamics Specialist Conference*, AAS 09-233, Pittsburgh, PA, 2009.

[13] Matthew D Hejduk and Daniel E Snow. The effect of neutral density estimation errors on satellite conjunction serious event rates. *Space Weather*, 16(7):849–869, 2018.